Defect imaging in layered composite plates and honeycomb sandwich structures using sparse piezoelectric transducers network

A Kulakovskyi, Olivier Mesnil, Alain Lhémery, B Chapuis, O D'almeida

IOP Conf. Series: Journal of Physics: Conf. Series **1184** (2019) 012001 doi:10.1088/1742-6596/1184/1/012001

Defect imaging in layered composite plates and honeycomb sandwich structures using sparse piezoelectric transducers network

A Kulakovskyi[1,2], O Mesnil[1], A Lhémery[1], B Chapuis[1], and O d'Almeida[2]

[1] CEA LIST, Gif-sur-Yvette, F-91191, France
[2] SAFRAN Tech, Magny-Les-Hameaux, F-78114, France

E-mail: olivier.mesnil@cea.fr

Abstract. Carbon fiber reinforced polymer (CFRP) plates and honeycomb composite sandwich structures (HCSS) are widely used in the aerospace industry as they exhibit excellent strength-to-weight ratio, stiffness, toughness, corrosion resistance, etc. Nevertheless, defects, such as face sheet delamination or core-sheet debonding, may appear due to the impact forces or thermo-mechanical aging and can degrade these properties. Structural health monitoring (SHM) based on the use of guided elastic waves (GW) is regarded as a promising solution to detect such defects, and consequently to reduce maintenance costs and to extend structure service time. GWs propagate over large distances while being sensitive to structural inhomogeneities. Here, a SHM system prototype is proposed. It relies on a sparse grid of piezoelectric transducers distributed over the structure, used for both actuating and sensing GWs. Defect imaging is performed by means of the correlation based algorithm, the so-called Excitelet. It computes correlation coefficients between the theoretical and experimental GW signals for each pixel on the image representing the region of interest of the structure. The theoretical signals for CFRP are computed using a model based on a 2D semi-analytical finite element formulation. Analytical prediction of theoretical signals for the HCSS being intractable, a homogenization model is applied to the honeycomb core to replace it by an equivalent orthotropic plate preserving the same modelling approach. Defect imaging results are presented for both structures, namely a CFRP plate and a HCSS. The resolution of the corresponding images can be related to the wavelength of the inspecting mode.

1. Introduction

The carbon fiber reinforced polymer (CFRP) plates and honeycomb composite sandwich structures (HCSS) have been largely employed in the aerospace industry since the 1950s. Their excellent mechanical properties, lightweight, and corrosion resistance make them very attractive for the use in the severe operational environment [1]. However, defects, such as woven composite plies delamination or core-sheet debonding, can appear due to the impact forces or thermo-mechanical aging so that stiffness properties may degrade [1-3]. This kind of defects often occurs within the structure. While being barely detectable on the composite surface to the naked eye, they can expand internally to large volumes up to the structure fails [4]. Moreover, such composite structures are often hardly accessible to maintenance teams performing the regular nondestructive examination. Manufacturers of composite structures introduce a safety margin design to resist accidental impacts and structure aging. This leads to the additional weight of the structure and to consequent economic shortcomings [5].

Aforementioned reasons became a driving force for the development of structural health monitoring system (SHM). It envisages accurate location and quantification of damages in composite structures

while being robust to environmental effects, such as temperature and humidity variations, accumulated strains, etc. SHM system can potentially replace scheduled maintenance, reduce safety margin design, and hence introduce significant economic benefits.

Guided elastic waves (GW) have been proven effective for inspecting industrial structure as they can propagate over large distances while being highly sensitive to structural inhomogeneities. Among other SHM methods, GWs can be easily actuated and sensed by a set of piezo-electric transducers attached to the surface while exciting the whole structure cross-section [2]. Numerous studies have been conducted on GWs propagation phenomenon. Theoretical and experimental works report on the relative simplicity of the GWs propagation in isotropic materials, whereas there is an additional complexity for composites structures. More specifically, there are effects of steering angle, energy focusing and even presence of energy band gaps for HCSS. Nevertheless, GWs ability for detecting cracks, delaminations, disbonding, and passing-through defects has been shown [2, 3].

Various GW imaging (GWI) algorithms, such as Delay-And-Sum, MVDR imaging, RAPID, have been developed [6-8]. While being effective for imaging defects in isotropic structures, their detection ability decreases when applied to anisotropic structures. On the other hand, defect imaging algorithm Excitelet turns into advantage the dispersive behavior of the structure, but requires a comprehensive understanding of GWs propagation and transducers dynamics [9].

This paper is organized as follows. Firstly, a brief review of GWI algorithms is presented. Then, our approach for simulating GWs propagation in CFRP plates and HCSS is described. GWI algorithm, namely Excitelet, is then used to compute images representing integrity of the structure. The results are illustrated and discussed, conclusions are drawn.

2. Defect imaging methodology

Guided Wave Imaging (GWI) is one of the most effective approaches to evaluate 'healthiness' of a structure. It employs an imaging algorithm in order to construct a cartography, where each pixel is mapped to the corresponding elementary portion of the structure [8]. Flaw presence, localization, and severity are deduced by analyzing the spatial intensity distribution on the cartography.

A schematic of the GWI process is represented in Figure 1. The grid of pixels discretizes the region of interest (ROI) of the studied specimen. In the current study, we use the demanding baseline algorithm Excitelet, which attributes a global Damage Index (DI) value to each pixel. Exploiting GWs propagation specificities, it processes residual signals measured by each pair of piezoelectric transducers (one emitter, one receiver) distributed over the structure [8, 9]. It is also assumed that the wavelength of excited GWs is of the same order of magnitude as the defect size in order to observe GWs scattering. Therefore, the residual signal, obtained as the difference between pristine and damaged states of the structure, contains echoes arising from the defect.

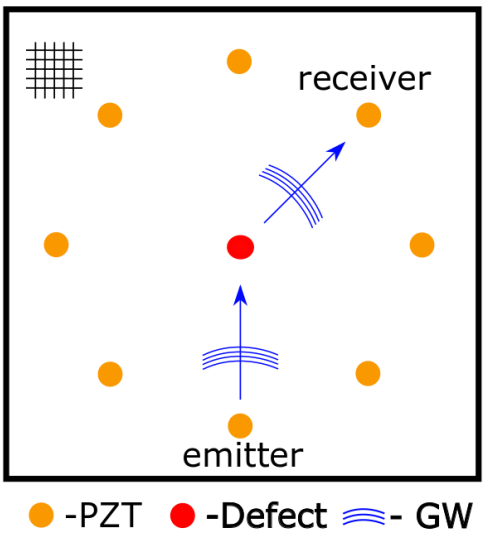

Figure 1: Illustration of the GWI methodology for defect cartography computation. GWs are excited and measured by the sparse set of the PZTs distributed over the structure.

The global DI value (1) is obtained as the sum of local DI_j (2) values computed for each PZT j[th] pair [9]. The latter is expressed as the modulus of a correlation coefficient between the experimental residual signal and the theoretical signal propagated from the emitter to the point of interest and from that point to the receiver.

$$DI(x_i, y_i) = \sum_j DI_j(x_i, y_i) \quad (1)$$

$$DI_j(x_i, y_i) = \left| \frac{\int_{t_0}^{t_{max}} S^{exp}_{emit_j \to rec_j}(t)\, S^{theor}_{emit_j \to rec_j}(t) dt}{\sqrt{\int_{t_0}^{t_{max}} \left(S^{exp}_{emit_j \to rec_j}(t) \right)^2 dt \int_{t_0}^{t_{max}} \left(S^{theor}_{emit_j \to rec_j}(t) \right)^2 dt}} \right|, \quad (2)$$

where $DI(x_i, y_i)$ denotes damage index value for a (x_i, y_i) pixel, $S^{exp}_{emit_j \to rec_j}(t)$ denotes the measured residual signal, and $S^{theor}_{emit_j \to rec_j}(t)$ denotes the theoretical signal for the corresponding PZT pair.

The theoretical signal can be calculated as a convolution of an excitation function with the Green's function (3) that describes GWs propagation in the structure of interest:

$$S^{theor}_{emit \to rec}(r, t) = u(t) * G_{emit \to obs}(\mathbf{r_1}, t) * G_{obs \to rec}(\mathbf{r_2}, t), \quad (3)$$

where $u(t)$ denotes the excitation signal, $G(\mathbf{r}, t)$ is the Green's function, $\mathbf{r_1}$ and $\mathbf{r_2}$ denote the position of the observation point relatively to the emitter and the position of the receiver relatively to the observation point, respectively.

3. Guided Waves simulation in CFRP and HCSS

Poisson and Kirchhoff's theories accurately describe extensional and flexural motions in the isotropic plate at low frequency [12]. For CFRP and HCSS plates, more sophisticated modelling tools are required. They must account for the angular dependency of phase and group velocities and energy focusing factor (*i.e.* Maris' factor) caused by the anisotropy of the structure. Here, we apply the modal expansion method coupled with the semi-analytical finite element (SAFE) modelling. This method allows linear decomposition of the 3D wavefield on propagating modes so that each mode can be independently used for defect imaging in the structure [13-17].

3.1 Modelling framework for layered composite structure

Assuming linearity, wave fields in the structure can be decomposed over guided modes (*i.e.* modal decomposition). The SAFE method is employed to compute modes in layered composite plates. This method imposes waveguide discretization in the transverse direction x_3, while the GWs propagation in the direction x_1 is expressed analytically, see Figure 2.

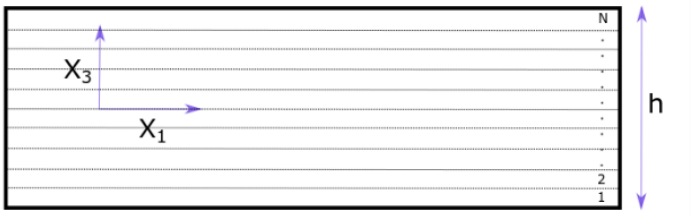

Figure 2: Schematic representation of layered waveguide. The GW propagates in x_1 direction while the waveguide discretized in x_3 direction.

More specifically, the two-dimensional Fourier transform according to the x_1 and t variables is applied to the equilibrium equation, while the x_3 direction is discretized following the usual Finite Element (FE) method. It results in the following matrix eigenproblem (4) [13]:

$$[k^2 A_2 + ikA_1 + A_0 - \omega^2 M]\underline{U} = 0, \quad (4)$$

where A_0, A_1, A_2 are the decomposition of the global stiffness matrix in power of k, M is the mass matrix, and U is the nodal displacement vector. These matrices are constructed from elementary matrices, which are computed for each element during the FE discretization procedure. Owing to the introduction of an auxiliary variable, the quadratic eigenproblem (4) is transformed into the linear eigenproblem (5), which can be solved by standard solvers for sparse matrices:

$$(A - kB)\underline{Q} = 0 \tag{5}$$
$$\underline{Q} = \begin{pmatrix} \underline{U} \\ k\underline{U} \end{pmatrix}$$

where

$$A = \begin{pmatrix} 0 & I \\ \omega^2 M - A_0 & -iA_1 \end{pmatrix} \qquad B = \begin{pmatrix} I & 0 \\ 0 & A_2 \end{pmatrix}.$$

Eigenvalues and eigenvectors obtained by solving equation (5) correspond to the wavenumbers and the modal displacements of guided modes. Solutions are obtained for both directions of propagation x_1 and $-x_1$, so the modes corresponding to the positive direction of propagation x_1 have to be extracted. Further filtering has to be applied to eliminate evanescent modes, for which the wavenumber is purely imaginary (i.e. $real(k) = 0\ rad/mm$), and rapidly decaying ones, for which the wavenumber has a significant imaginary part (i.e. $imag(k) > 1e^{-3}\ rad/mm$).

Once modes in the current waveguide are known, the Poynting vector (6), and consequently 2D Excitability matrix (7) for one given mode m can be computed from corresponding eigenvalues and eigenvectors for the angle ψ_m [16].

$$P_m(\theta) = \frac{\omega}{2} * \ imag\left(\underline{U_m}^*(\theta)(ikA_2 + A_4)\underline{U_m}(\theta)\right) \tag{6}$$
$$E_m^{2D}(\theta) = \frac{i\omega}{4P_m}\underline{U_m}(\theta)\ \underline{U_m}^*(\theta). \tag{7}$$

It has been shown [17] that far-field asymptotic expression of the 3D Green's function of the composite plate can be written in terms of the modal expansion. It allows reconstructing the 3D theoretical signal using 2D modal solutions computed by SAFE. The relation between 2D and 3D formulations of the guided waves is the following:

$$E_m^{3D}(\alpha, z) = B_m(\psi_m)A^{-1}(\psi_m){E_m}^{2D}(\psi_m)A(\psi_m), \tag{8}$$

where $B_m(\psi_m)$ is the propagation factor of the mode m in the direction ψ_m, $A(\psi_m)$ is a rotation matrix, and ψ_m is the steering angle of the guided mode m. Equation (8) shows that the far-field solution for the mode m in the α direction is related to the appropriate 2D modal solution for the same mode in the ψ_m direction. The 3D Green's function for the structure of interest can be expressed as follows:

$$G^{3D}(r, \alpha, z) = \frac{1}{\sqrt{r}}\sum_m E_m^{3D}(\alpha, z)e^{irk_m(\psi_m)Cos(\psi_m - \alpha)} \tag{9}$$

In order to compute each modal component of the 3D Green's function, it is necessary to track each mode for the frequency range of interest. A useful property of guided modes is that they form an orthogonal basis of the solutions in the waveguide section for a given frequency (4). An efficient way to check this property is to use the following orthogonality matrix [18]:

$$O_m = \begin{pmatrix} K_1 - \omega^2 M & 0 \\ 0 & -K_3 \end{pmatrix} \tag{10}$$

which represents a scalar product on a specific basis. Hence, the modal displacements obtained for the formulation (4) have to be expressed on this specific basis. The basis change is done through the unitary transformation matrix T (11). More specifically, the matrix T is eye-like, where all off-diagonal elements are equal to zero. The diagonal elements are equal to one, except for the elements corresponding to the particle displacements in $x_1$the direction that are equal to the imaginary unit i.

$$\underline{\check{Q}} = T\underline{Q} \tag{11}$$

Orthogonality relation states that for frequency ω all existing modes are orthogonal, which yields (12):

$$\underline{\check{Q}}_n^*(\omega)O_m(\omega)\underline{\check{Q}}_m(\omega) = 0 \tag{12}$$

Consequently, it can be assumed that orthogonality relation still approximately holds for the solutions that are quite close in the frequency domain, which gives:

$$\begin{cases} \underline{\check{Q}}_n^*(\omega)O_m(\omega)\underline{\check{Q}}_m(\omega+\Delta\omega) \approx 0 \\ \underline{\check{Q}}_m^*(\omega)O_m(\omega)\underline{\check{Q}}_m(\omega+\Delta\omega) \neq 0 \end{cases} \tag{13}$$

Orthogonality terms have to be calculated between the current eigenvector $\underline{\check{Q}}_m(\omega)$ that corresponds to the mode m at frequency ω and all other existing solutions for adjacent frequency $\underline{\check{Q}}_m(\omega+\Delta\omega)$. The correct mode continuation is achieved by maximization of the orthogonality term while performing mode sorting procedure. More details on SAFE formulation used herein can be found in Refs. [13-15].

3.2 Honeycomb core homogenization

The honeycomb sandwich structure consists of the aluminum honeycomb core bonded with adhesives to the composite skins (see

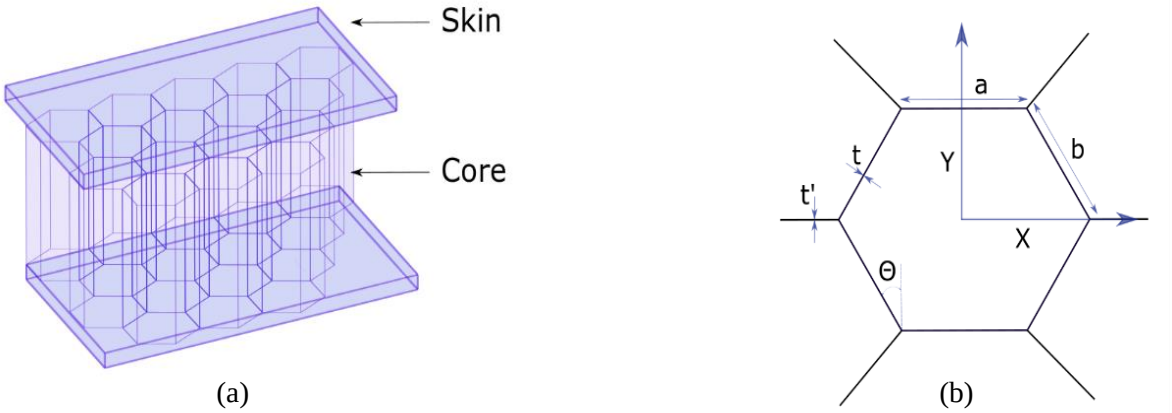

(a) (b)

Figure 3). Such a complex structure cannot be straightforwardly modelled by SAFE formulation. To do this, the complex periodic structure of the HCSS core is homogenized and replaced in the SAFE computation by an equivalent orthotropic layer having the same thickness as that of the core. Such a procedure allows considering an HCSS structure as a multi-layered composite plate, and hence to compute modes by SAFE. It is worth noting that the accuracy of the computed results is only ensured at low frequencies, where the wavelength of the propagating mode is larger than honeycomb cell size [16].

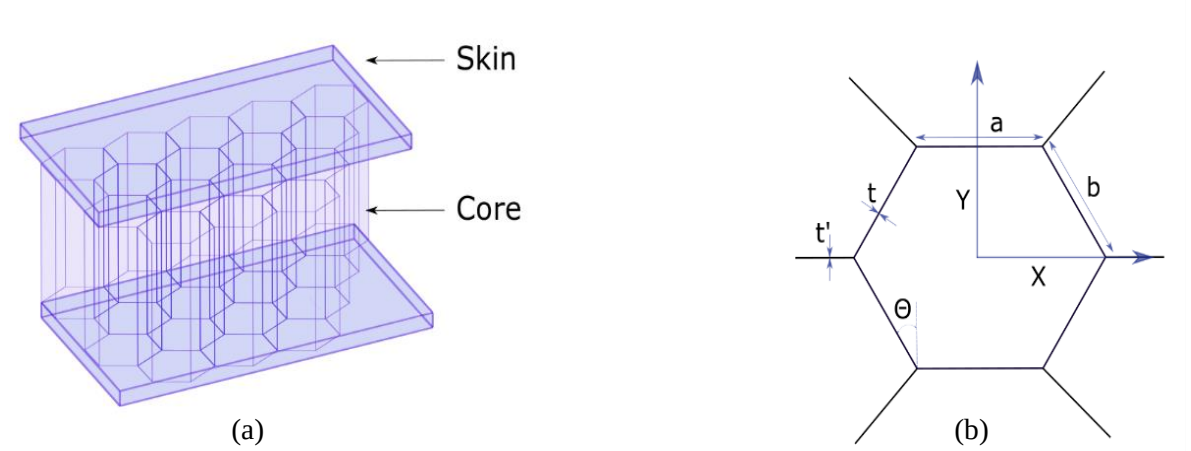

Figure 3: (a) Schematic representation of a honeycomb sandwich structure. (b) Geometric parameters of the unit honeycomb cell. The side lengths of the cell are defined by a and b, while the single wall and double wall thicknesses are defined by t and t', respectively.

The Gibson and Ashby's model is considered as a reference work for the honeycomb core homogenization [17, 18]. It permits computing nine elastic effective parameters (Young moduli, shear moduli and Poisson ratios) of an equivalent orthotropic plate. This analytical model requires the geometric parameters of the honeycomb cell, shown in

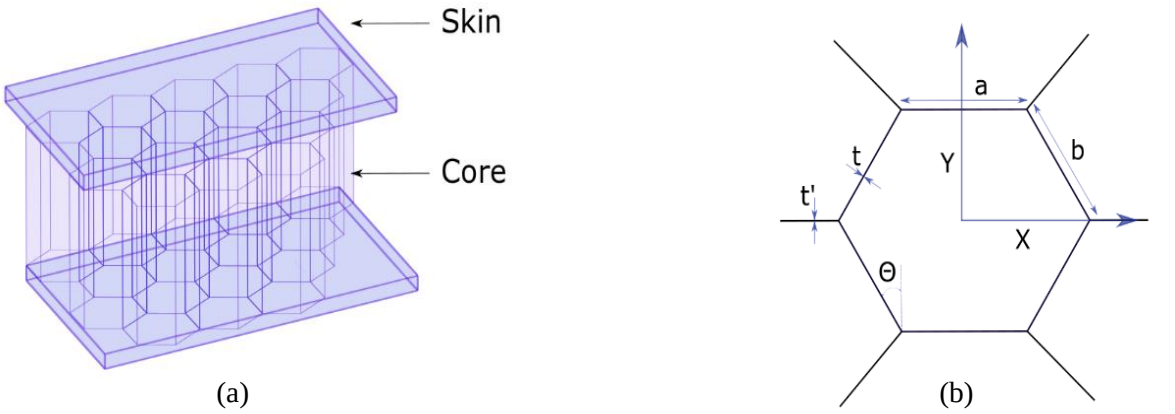

Figure 3b, and elastic properties of the constituting material to be known. The model ignores vertices at the intersection of horizontal and inclined walls of the cell and neglects the double thickness of the walls in the X direction. It does not predict well measurements for increasing value of the relative density of the core.

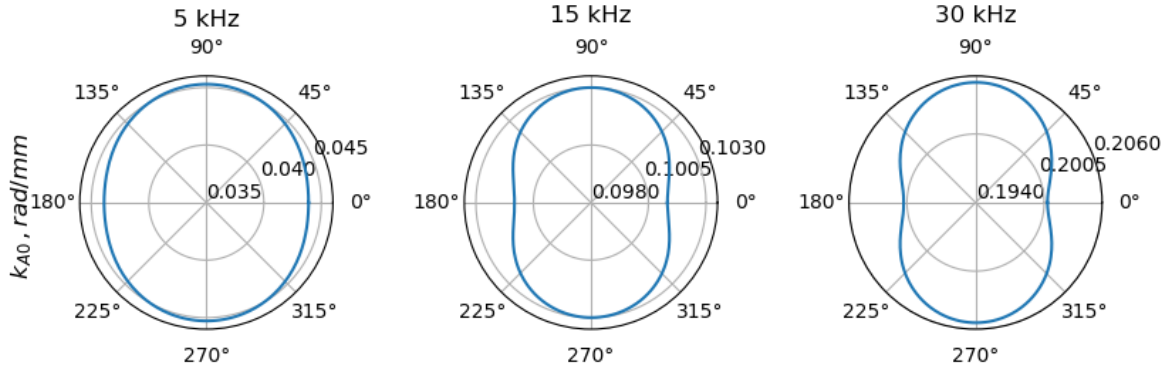

Figure 4: Wavenumber diagrams of A0 mode at 5 kHz, 15 kHz and 30 kHz. At 5 kHz the propagation is almost omnidirectional, though the anisotropy of GWs propagation increases with the frequency.

In their recent work, Malek and Gibson overcame this problem by considering honeycomb cell vertices and by introducing an effective bending length of cell walls, which resulted in a more accurate analytical model [18]. Hence, this model has been agreed for this study. It has been shown that the effective shear moduli G_{xz} and G_{yz} of the core and the Young modulus of the skins have the highest impact on the HCSS dynamics.

4. Imaging results

The orthotropic CFRP plate (1000 mm x 600 mm x 5.775 mm) and the HCSS (1000 mm x 600 mm x 20.7 mm) are selected for the study. Each woven-ply CFRP is oriented in the 0° direction. The HCSS top skin consists of two CFRP and one E-glass plies, while the bottom skin is made of four CFRP and one E-glass plies. Corresponding elastic parameters are tabulated in the table:

Table 1: Elastic parameters of the orthotropic CFRP, E-glass plies, and effective elastic parameters the of honeycomb core obtained via a homogenization model.

	$\mathbf{E_1 = E_2}$ **(MPa)**	$\mathbf{E_3}$ **(MPa)**	$\boldsymbol{\nu_{12}}$	$\boldsymbol{\nu_{13} = \nu_{23}}$	$\mathbf{G_{12}}$ **(MPa)**	$\mathbf{G_{13} = G_{23}}$ $(\boldsymbol{MPa})$	$\boldsymbol{\rho}$ $\left(\mathbf{Kg/m^3}\right)$
CFRP	65700	4500	0.03	0.3	5100	2500	1760
Core	0.4	1131.3	0.8	0.00013	0.1	207.2	67
E-glass	72400			0.255	28800		2100

The model presented above has been used to build a dictionary of the 3D Green's function for both the woven-ply CFRP plate and the HCSS. Polar plots of the wavenumber, phase and group velocities computed at 5 kHz, 15 kHz and 30 kHz for HCSS are shown in

Figure 4. Note that the variation of the wavenumber is small, so the considered HCSS structure exhibits a quasi-isotropic behavior in the plate plane. Both structures are similarly instrumented with piezo-electric transducers for GWs actuating and sensing. The presence of a defect is simulated by an attached mass of 200 g, which is coupled to the surface using coupling gel. The woven-ply CFRP plate with eight attached PZT 13 mm in diameter forming a octagon 200 mm in diameter is first used in the experiments, and results are shown in Figure 5a. The Hanning modulated two cycles (at 40 kHz) burst is selected for the excitation of emitters function for the woven-ply CFRP plate inspection.

A similar set-up is then used to perform guided waves imaging in the HCSS. Six PZT 13 mm in diameter are distributed over the surface, forming a hexagon 300 mm in diameter (see the schematic shown in Figure 6). The excitation function contains three Hanning modulated cycles set to 15 kHz. GWs are measured following the round-robin process for both pristine and damaged states. For example, in Figure 6 the pristine and damaged signals and corresponding residual signals are shown for the $PZT_{1\text{-}5}$ pair.

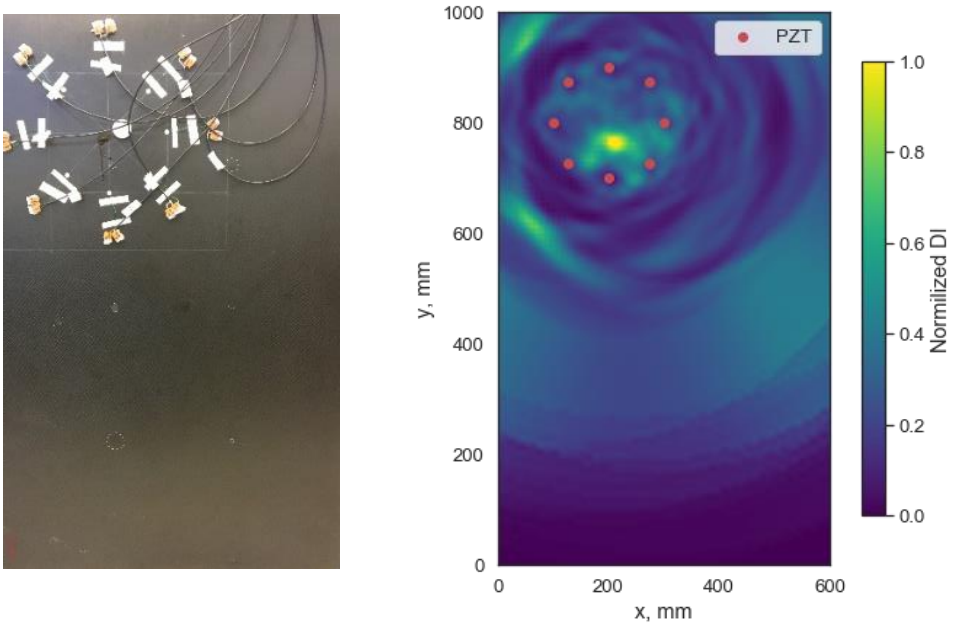

(a) (b)

Figure 5: (a) 8 PZT sparse array serves for GWs actuation and sensing. (b) Virtual defect imaging on woven-ply CFRP in order to validate the imaging algorithm.

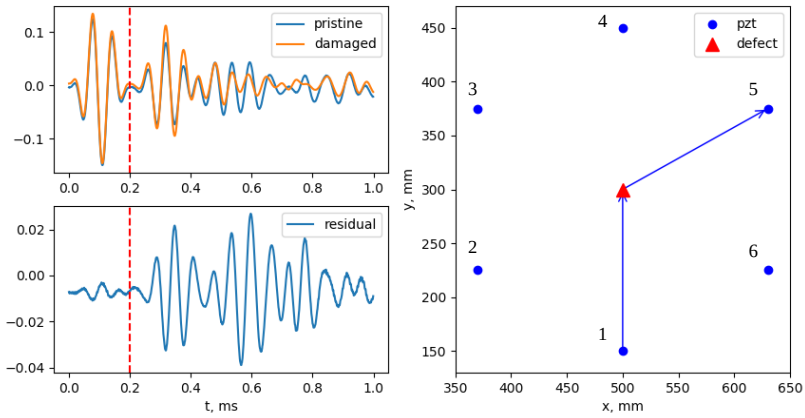

Figure 6: Schematic representation of signal processing by defect imaging algorithm. Signals for the pristine and damage states, and corresponding residual signal are shown in the left column for the GWs propagating from the 1st to the 5th transducers.

Our signal acquisition system suffers from electromagnetic coupling in the multiplexer (the part of the time series appearing before the red dashed line on the top image to the left), which is almost constant during the acquisition process. Once all the residual signals have been collected, the defect imaging is performed by means of Excitelet algorithm in the single-mode regime (A_0 mode being selected). The defect imaging result in the orthotropic CFRP plate is presented in Figure 5b, while Figure 7b shows the image obtained in the HCSS.

The spatial intensity distribution of DI on the cartography is directly related to the wavelength of the propagating guided mode. In the present study, the HCSS was inspected by A_0 mode at 15 kHz with the

wavelength $\lambda_{A0}^{HCSS} = 63\ mm$, while the woven-ply CFRP plate was monitored at 40 kHz with the same mode and the corresponding wavelength $\lambda_{A0}^{CFRP} = 32\ mm$.

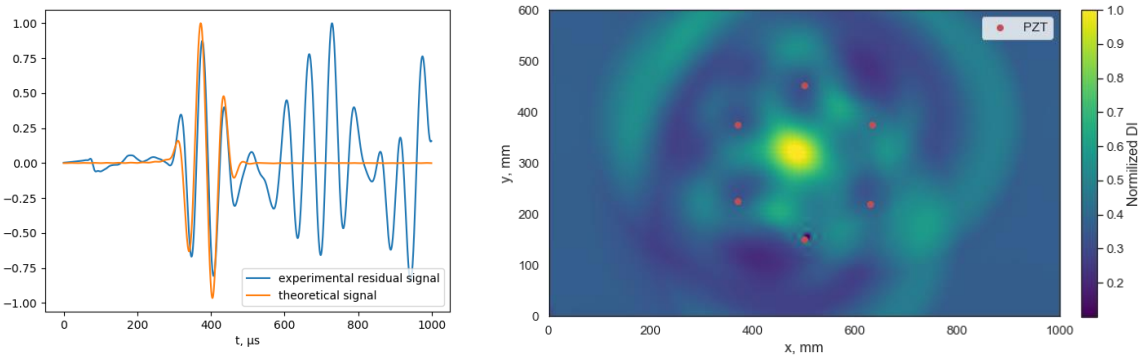

(a) (b)

Figure 7: (a) Residual experimental signal is compared to the theoretical signal propagated from the emitter to the potential defect location and from latter to the receiver. (b) Cartography computed by mean of Excitelet imaging algorithm.

Doubling the wavelength leads to the decrease of the resolution capability of the defect imaging algorithm. To achieve higher resolution, it is thus necessary to inspect structures in a higher frequency range to decrease the wavelength of the mode chosen for imaging. Considering the imaging algorithm used in our study, this implies that the corresponding 3D Green's function must be predicted with high accuracy in this frequency range.

However, the honeycomb homogenization model, which substitutes a honeycomb core with an equivalent orthotropic plate, is no longer valid at frequencies where the wavelength is comparable to the size of the honeycomb cell. In this case, guided modes become sensitive to the inner periodicity of the structure and propagate in HCSS as Bloch's waves in phononic crystals [19].

5. Conclusions

This paper reports on the guided wave defect imaging in woven-ply CFRP plate and HCSS. Defect image is obtained by means of a correlation-based algorithm, the so-called Excitelet. It requires to obtain the residual signal from the experimental and predicted signals of the inspected structure. While the first one is measured by the sparse set of piezo-electric transducers, the latter has to be modelled taking into account the dispersive nature of guided waves in plate-like structures. In the current work, we used the modal expansion method coupled with the 2D SAFE method to compute the 3D wavefield. Analytical homogenization for the honeycomb core was applied to replace the periodic core for an equivalent orthotropic layer. This allows us to compute modes in the HCSS using SAFE by treating it as a multi-layered structure.

By comparing results for defect cartographies in woven-ply CFRP plate and in HCSS, it can be deduced that image resolution highly depends on the excited wavelength. In the CFRP plate, the wavelength at the inspected frequency is about 32 mm, while that in the HCSS is about 63 mm. Hence, the image resolution in case of CFRP plate is higher than in case of HCSS. Unfortunately, analytical homogenization model is only valid in the low-frequency regime, and the quality of the elastodynamic predictions rapidly decreases while the frequency increases.

For further studies, we will focus on the use of finite element modelling to compute effective elastic parameters in order to reach higher accuracy in defect localization. We will also focus on experimental approaches to measure the 3D Green's function for the HCSS. Multi-mode defect imaging with Excitelet algorithm for woven-ply CFRP plates and HCSS is also in the scope of interest for further studies.

6. References

[1] Menna C, Zinno A, Asprone D and Prota A 2013 *Composite Structures* **106** 326-39
[2] Mitra M and Gopalakrishnan S 2016 *Smart Mater. Struct.* **25** 053001

[3] Song F and Huang G L and Hudson K 2009 *Smart Mater. Struct.* **18** 125007
[4] Aktay L, Johnson A F and Holzapfel M 2005 *Computation. Mater. Science* **32** 252-60
[5] Lazarević I and Petrović Z 2015 *Scientific Techn. Rev.* **65** 45-52
[6] Hettler J, Tabatabaeipour M, Delrue S and Van Den Abeele K 2016 *Materials* **9** 901-17
[7] Levine R, Michaels J E and Lee S J 2012 *AIP Conference Proceedings* **1430** 647-654
[8] Li P, Zhu X, Luo C and Deng F 2015 *Trans. Institute Measurement Control* **37** 1274-81
[9] Ostiguy P C, Quaegebeur N and Masson P 2014 Damage detection, localization and size estimation using broadband correlation-based imaging, *EWSHM 2014 conference proceedings* published on-line *http://www.ndt.net/article/ewshm2014/papers/0147.pdf*
[10] Su Z, Ye L and Lu Y 2006 *J. Sound Vib.* **295** 753-80
[11] Quaegebeur N, Masson P, Langlois-Demers D and Micheau P 2011 *Smart Mater. Struct.* **20** 02005
[12] Deng Q and Yang Z 2011 *Appl. Math. Modelling* **35** 550-62
[13] Chapuis B, Terrien N and Royer D 2010 *J. Acoust. Soc. Am.* **127** 198-203
[14] Taupin L, Lhémery A and Inquiété G 2011 *J. Phys.: Conf. Ser.* **269** 012002
[15] Stévenin M, Lhémery A and Grondel S 2016 *J. Phys.: Conf. Ser.* **684** 012004
[16] Song F, Huang G L and Hudson K 2009 *Smart Mater. Struct.* **18** 125007
[17] Gibson J and Ashby F 2001 *Cellular Solids, Structure and Properties* (Cambridge: Cambridge University Press)
[18] Malek S and Gibson L 2015 *Mech. Mater.* **91** 226-40
[19] Tie B, Tian B Y and Aubry D 2016 *J. Sound Vib.* **382** 100-21